

1           **Rheologic constraints on the upper mantle from five years of**  
2           **postseismic deformation following the El Mayor-Cucapah**  
3           **earthquake**

4           **T. T. Hines<sup>1</sup>, E. A. Hetland<sup>1</sup>**

5           <sup>1</sup>Department of Earth and Environmental Sciences, University of Michigan, Ann Arbor, Michigan, USA.

6           **Key Points:**

- 7           • = enter point 1 here =  
8           • = enter point 2 here =  
9           • = enter point 3 here =

10 **Abstract**

11 Five years of postseismic deformation following the Mw7.2 El Mayor-Cucapah earthquake re-  
 12 veals transient deformation that decays back to its pre-earthquake trend after  $\sim 3$  years at epi-  
 13 central distances greater than  $\sim 200$  km. At closer distances, the rapid transience decays to a  
 14 sustained rate which exceeds its pre-earthquake trend. We attempt to determine the mecha-  
 15 nisms driving this deformation, where we consider afterslip at seismogenic depths and viscoelas-  
 16 tic relaxation in the lower crust and upper mantle as candidate mechanisms. We find that early,  
 17 rapid, near-field deformation can be explained with afterslip on the fault that ruptured coseis-  
 18 mically, while the later, sustained, near-field deformation can be explained with either contin-  
 19 ued afterslip in an effectively elastic lower crust, or lower crustal viscoelastic relaxation with  
 20 a steady-state viscosity of  $\sim 10^{19}$  Pa s. The trend in far-field deformation is best explained with  
 21 a transient viscosity of  $\sim 10^{18}$  Pa s in the upper mantle. We argue that a transient rheology  
 22 in the mantle is preferable over a Maxwell rheology because it better predicts the decay in post-  
 23 seismic deformation, and also because it does not conflict with the generally higher, steady-  
 24 state viscosities inferred from studies of geophysical processes occurring over longer time-scales.

25 **1 Introduction**

26 Ground deformation in the years following a large ( $\gtrsim$ Mw7) earthquake provides insight  
 27 into the mechanical behaviour of the crust and upper mantle. It has long been recognized that  
 28 interpretations of postseismic deformation can be ambiguous because multiple postseismic de-  
 29 formation mechanisms can have qualitatively similar surface expressions [e.g. Savage, 1990].  
 30 Owing to the dense geodetic network deployed throughout the 2000s as part of the Plate Bound-  
 31 ary Observatory, the postseismic deformation following the April 4, 2010, Mw7.2 El Mayor-  
 32 Cucapah earthquake in Baja California was observed at more GPS stations than any other earth-  
 33 quake in California to date. With such a large collection of data, we attempt to discern the mech-  
 34 anisms driving postseismic deformation following the El Mayor-Cucapah earthquake, where  
 35 we consider both afterslip and viscoelastic relaxation in the lower crust and upper mantle as  
 36 candidate mechanisms.

37 Previous studies which have modelled postseismic deformation following the El Mayor-  
 38 Cucapah earthquake include Pollitz *et al.* [2012], Gonzalez-Ortega *et al.* [2014], Spinler *et al.*  
 39 [2015], and Rollins *et al.* [2015]. Of these studies, Gonzalez-Ortega *et al.* [2014] and Rollins  
 40 *et al.* [2015] have attempted to describe the postseismic deformation with afterslip in an elas-  
 41 tic half-space. Gonzalez-Ortega *et al.* [2014] described five months of postseismic deforma-  
 42 tion, observed by InSAR and GPS within  $\sim 50$  km rupture, with afterslip and contraction on  
 43 the coseismically ruptured fault. Gonzalez-Ortega *et al.* [2014] noted that their preferred model  
 44 underestimated the GPS displacements for stations  $\gtrsim 25$  km from the rupture and suggested  
 45 that it could be the result of unmodelled viscoelastic relaxation. Using only continuous GPS  
 46 stations, which are mostly north of the rupture zone, Rollins *et al.* [2015] found that three years  
 47 of postseismic deformation can be adequately explained by afterslip, albeit with an implau-  
 48 sibly large amount of slip inferred on the least constrained, southern-most fault segment. Here,  
 49 we suggest the afterslip inferred by Rollins *et al.* [2015] may have been acting as a proxy for  
 50 distributed relaxation in the upper mantle.

51 Pollitz *et al.* [2012], Rollins *et al.* [2015] and Spinler *et al.* [2015] have explored viscoelas-  
 52 tic relaxation in the lower crust and upper mantle as a potential postseismic deformation mech-  
 53 anism. The rheology of the crust and mantle is largely unknown and so modelling postseis-  
 54 mic deformation with viscoelastic relaxation requires one to assume a rheologic model and  
 55 then find the best fitting rheologic parameters. The inference of these rheologic parameters is  
 56 a computationally expensive non-linear inverse problem which is typically approached with  
 57 a forward modelling grid search method. Consequently, a simplified structure for the lithosphere  
 58 must be assumed in order to minimize the number of rheologic parameters that need to be es-  
 59 timated. For example, it is commonly assumed that the lithosphere consists of only three ho-  
 60 mogeneous, Maxwell viscoelastic layers, which may be an inadequate representation of the

lithosphere [Riva and Govers, 2009; Hines and Hetland, 2013]. To further reduce the dimensions of the model space, it is also necessary to make simplifying assumptions about the nature of afterslip. For example, one can assume a frictional model for afterslip and parametrize afterslip in terms of the unknown rheologic properties of the fault [e.g. Johnson *et al.*, 2009; Johnson and Segall, 2004]. One can also assume that afterslip does not persist for more than a few months and then model the later postseismic deformation assuming it to be the result of only viscoelastic relaxation [e.g. Pollitz *et al.*, 2012; Spinler *et al.*, 2015]. However, postseismic afterslip in similar tectonic settings has been observed to persist for decades following earthquakes [Çakir *et al.*, 2012; Cetin *et al.*, 2014]. Indeed, the preferred viscoelastic model from Pollitz *et al.* [2012] significantly underestimates deformation in the Imperial Valley, which could be indicative of unmodelled continued afterslip. Neglecting to allow for sustained afterslip as a postseismic mechanism could then lead to biased inferences of lithospheric viscosities.

In this study, we assume that both afterslip and viscoelastic relaxation can contribute to postseismic deformation. Modelling both of these mechanisms creates a high dimensional model space that must be searched with non-linear optimization methods. We first develop an initial postseismic model using the method described in Hines and Hetland [2016]. This method simultaneously estimates the afterslip and effective lithospheric viscosity structure necessary to describe early postseismic deformation. Our initial model describes the first 0.8 years of postseismic deformation following the El Mayor-Cucapah earthquake. We then use the inferred effective viscosity structure from the initial model to create a suite of postseismic models to explain the 5 years of postseismic data available to date. Of the suite of models tested, we find that postseismic deformation following the El Mayor-Cucapah earthquake can be explained with afterslip on a fault segment running through the Sierra Cucapah, a Zener rheology in the upper mantle with a transient viscosity that decays from  $5 \times 10^{18}$  Pa s to  $1 \times 10^{18}$  Pa s at 120 km depth, and a relatively stronger lower crust.

## 2 Data Processing

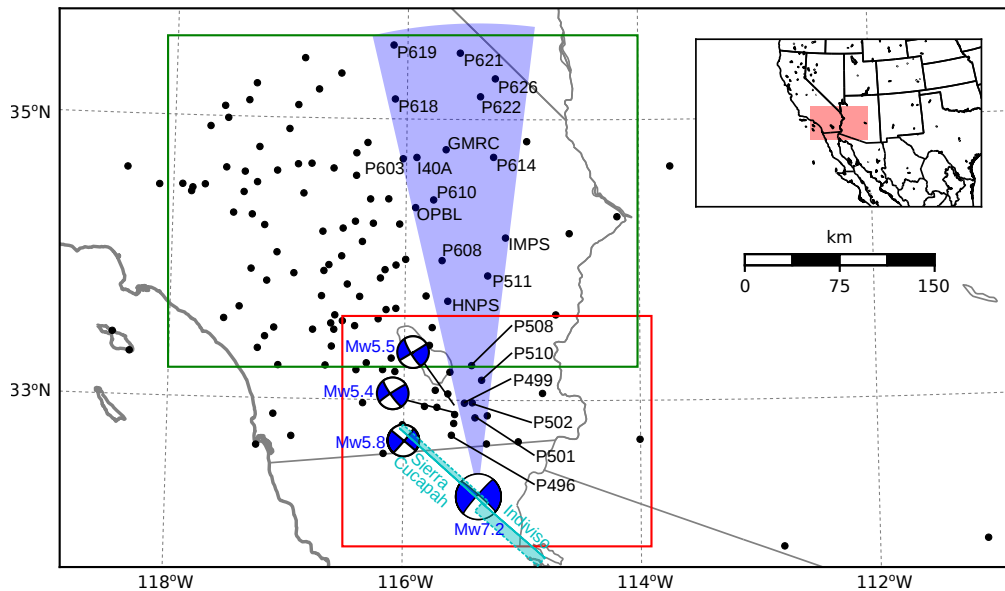
We use continuous GPS position time series provided by University Navstar Consortium (UNAVCO) for stations within a 400 km radius about the El Mayor-Cucapah epicentre. We collectively describe the coseismic and postseismic displacements resulting from the El Mayor-Cucapah earthquake as  $u_{\text{post}}(t)$ . We consider the GPS position time series,  $u_{\text{obs}}(t)$ , to be the superposition of  $u_{\text{post}}(t)$ , secular tectonic deformation, annual and semi-annual oscillations, and coseismic offsets from significant earthquakes over the time span of this study. The June 14, 2010, Mw5.8 Ocotillo earthquake and the Brawley swarm, which included an Mw5.5 and an Mw5.3 event on August 26, 2012, (Figure 1) are the only earthquakes that produced noticeable displacements in any of the time series. We treat the displacements resulting from the Brawley swarm as a single event because the daily solutions provided by UNAVCO cannot resolve the separate events. Although the Ocotillo earthquake had its own series of aftershocks [Hauksson *et al.*, 2011], neither the Ocotillo earthquake nor the Brawley swarm produced detectable postseismic deformation, and we model displacements resulting from these events with only a Heaviside function,  $H(t)$ , describing the coseismic offsets. We then model  $u_{\text{obs}}(t)$  as

$$u_{\text{obs}}(t) = u_{\text{pred}}(t) + \epsilon, \quad (1)$$

where

$$\begin{aligned} u_{\text{pred}}(t) = & u_{\text{post}}(t)H(t - t_{\text{emc}}) + c_0 + c_1 t + \\ & c_2 \sin(2\pi t) + c_3 \cos(2\pi t) + c_4 \sin(4\pi t) + c_5 \cos(4\pi t) + \\ & c_6 H(t - t_{\text{oc}}) + c_7 H(t - t_{\text{bs}}). \end{aligned} \quad (2)$$

In the above equations,  $t_{\text{emc}}$ ,  $t_{\text{oc}}$  and  $t_{\text{bs}}$  are the times of the El Mayor-Cucapah earthquake, Ocotillo earthquake, and the Brawley swarm, respectively,  $c_0$  through  $c_7$  are unknown coefficients, and  $\epsilon$  is the observation noise. We only estimate jumps associated with the Ocotillo earthquake and Brawley swarm for stations within 40 km of their epicentres.



87 **Figure 1.** Map of the region considered in this study. The large focal mechanism is for the El Mayor-  
 88 Cucapah earthquake and the three small focal mechanisms are for the Ocotillo earthquake and the two main  
 89 shocks during the Brawley swarm. The black dots indicate the locations of GPS stations used in this study.  
 90 The fault geometry used in this study is shown in cyan where dashed lines indicate buried edges of the fault  
 91 segments. The green and red boxes demarcate the extent of the near-field and far-field maps (figures 4 and 5).  
 92 Stations within the blue sector, which highlights the area within  $10^\circ$  of the El Mayor-Cucapah P axis, are used  
 93 in the record sections in Figures 7, 10, and 14

99 Stations which recorded displacements that clearly cannot be described by the aforementioned  
 100 processes are not included in our analysis. This includes stations in the Los Angeles  
 101 basin, where anthropogenic deformation can be larger than the postseismic signal that we are  
 102 trying to estimate [Bawden *et al.*, 2001; Argus *et al.*, 2005]. In order to ensure an accurate es-  
 103 timation of the secular deformation, we only use stations that were installed at least six months  
 104 prior to El Mayor-Cucapah earthquake. Several GPS stations were installed after the El Mayor-  
 105 Cucapah earthquake to improve the spatial resolution of postseismic deformation [Spinler *et al.*,  
 106 2015]. Although it would be possible to subtract secular velocities derived from elastic block  
 107 models [e.g. Meade and Hager, 2005] from velocities recorded at the newly installed stations  
 108 to get an estimate of postseismic velocities, we do not do so here. We use coseismic and post-  
 109 seismic displacements, rather than velocities, in our inverse method described in Section 3. We  
 110 use displacements because estimating velocities from an already noisy displacement time se-  
 111 ries can introduce significant uncertainties depending on exactly how the estimation is done.  
 112 This choice prevents us from using the newly installed stations in Baja California for our anal-  
 113 ysis.

114 The October 16, 1999, Mw7.1 Hector Mine earthquake, which occurred  $\sim$ 270 km north  
 115 of the El Mayor-Cucapah epicentre, produced transient postseismic deformation which we do  
 116 not wish to model, either mechanically or through empirical line fitting. We thus restrict our  
 117 analysis to deformation observed six years after the Hector Mine earthquake, which is when  
 118 postseismic velocities at sites proximal to the Hector Mine epicentre are approximately con-  
 119 stant [Savage and Svare, 2009]. When appraising our model fit in Section 3, we see some sys-  
 120 tematic residuals in the vicinity of the Hector Mine epicentre, which may be the result of er-  
 121 rors in the assumption that the trend in Hector Mine postseismic deformation is linear after  
 122 six years.

Studies of postseismic deformation typically assume a parametric form for  $u_{\text{post}}(t)$ , such  
 as one with a logarithmic or exponential time dependence [e.g. Savage *et al.*, 2005]. However,  
 by assuming a logarithmic or exponential form of  $u_{\text{post}}(t)$  we run the risk of over fitting the  
 GPS time series and inferring a non-existent postseismic signal. We therefore do not assume  
 any parametric form for  $u_{\text{post}}(t)$  and rather treat it as integrated Brownian motion, so that

$$\dot{u}_{\text{post}}(t) = \sigma^2 \int_0^t w(s) ds, \quad (3)$$

where  $w(t)$  is white noise and the variance of  $\dot{u}_{\text{post}}(t)$  increases linearly with time by a fac-  
 tor of  $\sigma^2$ . We use a Kalman filtering approach to estimate  $u_{\text{post}}(t)$  and the unknown param-  
 eters in eq. (2). In the context of Kalman filtering, our time varying state vector is

$$\mathbf{X}(t) = [u_{\text{post}}(t), \dot{u}_{\text{post}}(t), c_0, \dots, c_7] \quad (4)$$

and eq. (2) is the observation function which maps the state vector to the GPS observations.  
 We initiate the Kalman filter by assuming a prior estimate of  $\mathbf{X}(t)$  at the first time epoch, de-  
 noted  $\mathbf{X}_{1|0}$ , which has a sufficiently large covariance, denoted  $\Sigma_{1|0}$ , to effectively make our  
 prior uninformed. For each time epoch,  $t_i$ , Bayesian linear regression is used to incorporate  
 GPS derived estimates of displacement with our prior estimate of the state,  $\mathbf{X}_{i|i-1}$ , to form  
 a posterior estimate of the state,  $\mathbf{X}_{i|i}$ , which has covariance  $\Sigma_{i|i}$ .

We then use the posterior estimate of the state at time  $t_i$  to form a prior estimate of the  
 state at time  $t_{i+1}$  through the transition function

$$\mathbf{X}_{i+1|i} = \mathbf{F}_{i+1} \mathbf{X}_{i|i} + \delta_{i+1} \quad (5)$$

where

$$\mathbf{F}_{i+1} = \begin{bmatrix} 1 & (t_{i+1} - t_i) & \mathbf{0} \\ 0 & 1 & \mathbf{0} \\ \mathbf{0} & \mathbf{0} & \mathbf{I} \end{bmatrix} \quad (6)$$

and  $\delta_{i+1}$  is the process noise, which has zero mean and covariance described by

$$\mathbf{Q}_{i+1} = \sigma^2 \begin{bmatrix} \frac{(t_{i+1}-t_i)^3}{3} & \frac{(t_{i+1}-t_i)^2}{2} & \mathbf{0} \\ \frac{(t_{i+1}-t_i)^2}{2} & (t_{i+1}-t_i) & \mathbf{0} \\ \mathbf{0} & \mathbf{0} & \mathbf{0} \end{bmatrix}. \quad (7)$$

The covariance of the new prior state,  $\mathbf{X}_{i+1|i}$ , is then described by

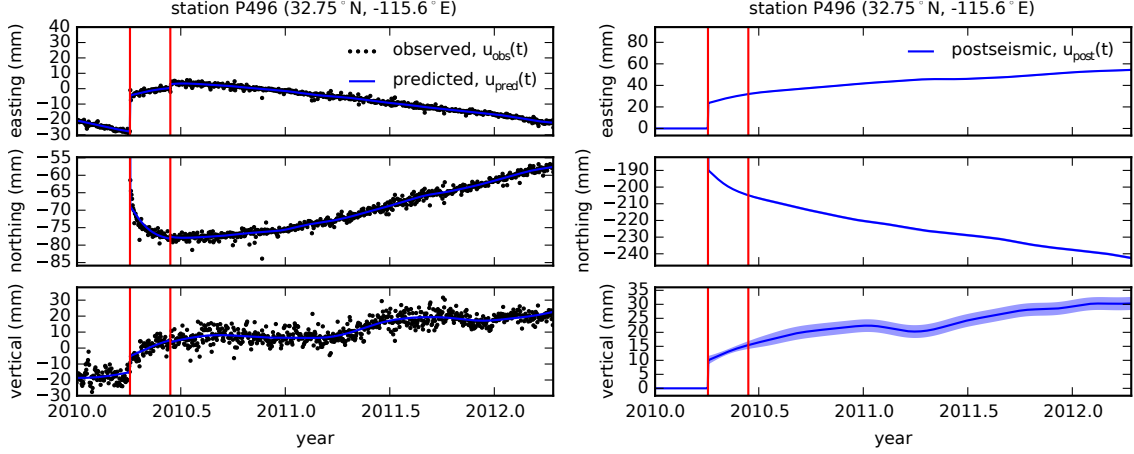
$$\Sigma_{i+1|i} = \mathbf{F}_{i+1} \Sigma_{i|i} \mathbf{F}_{i+1}^T + \mathbf{Q}_{i+1}. \quad (8)$$

This process is repeated for each of the  $N$  time epochs at which point we use Rauch-Tung-Striebel smoothing [Rauch *et al.*, 1965] to find  $\mathbf{X}_{i|N}$ , which is an estimate of the state at time  $t_i$  that incorporates GPS observation for all  $N$  time epochs. Our final estimates of  $u_{\text{post}}(t)$  are used in subsequent analysis, while the remaining components of the state vector are considered nuisance parameters. In the interests of computational tractability, we down sample our smoothed time series from daily solutions down to weekly solutions.

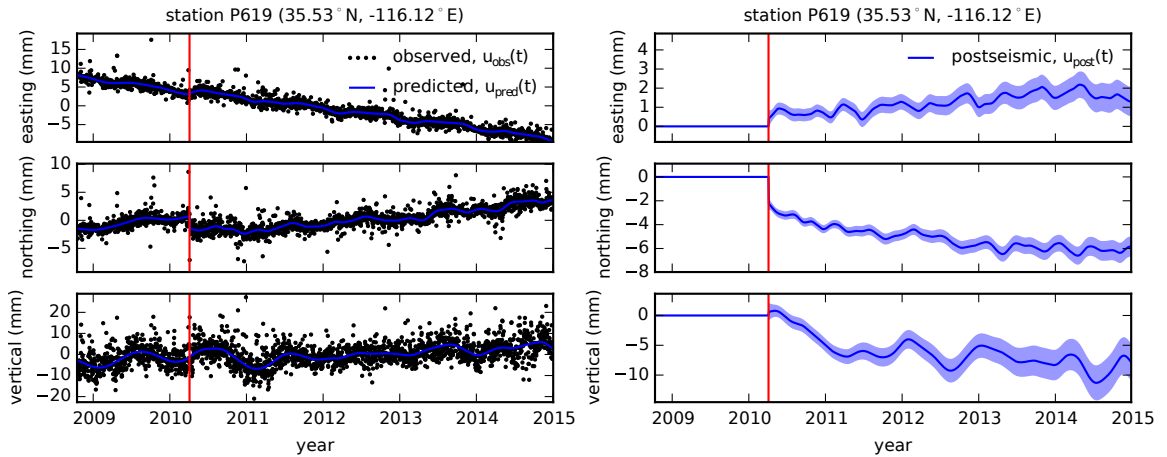
The smoothness of  $u_{\text{post}}(t)$  is controlled by the chosen value of  $\sigma^2$ , which describes how rapidly we expect postseismic displacements to vary over time. Setting  $\sigma^2$  equal to zero will effectively result in modelling  $u_{\text{post}}(t)$  as a straight line which is insufficient to describe the expected transient behaviour in postseismic deformation. The other end member, where  $\sigma^2$  is infinitely large, will result in  $u_{\text{pred}}(t)$  over fitting the data. While one can use a maximum likelihood based approach for picking  $\sigma^2$  [e.g. Segall and Mathews, 1997], we instead take a subjective approach and choose a value for  $\sigma^2$  that is just large enough to faithfully describe the observed deformation at the most near-field station in our study, P496, which exhibits the most pronounced rapid changes in velocity. This ensures that  $\sigma^2$  will be sufficiently large so that our estimate of  $u_{\text{post}}(t)$  does not smooth out potentially valuable postseismic signal at the remaining stations. We find that using  $\sigma^2 = 0.05 \text{m}^2/\text{yr}^3$  adequately describe all but the first week of postseismic deformation at station P496, which gets incorporated into our estimate of coseismic displacements (Figure 2). By down sampling, we implicitly assume that the first week of deformation is overwhelmingly the result of afterslip and this afterslip is lumped into our estimates of coseismic slip. Freed *et al.* [2007] noted that postseismic deformation can be observed at distances greater than 200 km from the Hector Mine earthquake and, after filtering the time series for stations up to 400 km from the El Mayor-Cucapah epicentre, we also clearly see far reaching postseismic transient deformation (Figure 3).

It is important to note that the shown uncertainties in  $u_{\text{post}}(t)$  do not account for the non-negligible epistemic uncertainty in eq. (2). For example, we assume a constant rate of secular deformation, which appears to be an appropriate approximation for all but perhaps the stations closest to the Hector Mine epicentre, as noted above. Also, our model for seasonal deformation in eq. (2) assumes a constant amplitude over time, which means that any yearly variability in the climatic conditions could introduce systematic residuals [Davis *et al.*, 2012]. Indeed, it would be more appropriate to consider the seasonal amplitudes  $c_2 - c_5$  in eq. (2) as stochastic variables [Murray and Segall, 2005]. By using constant seasonal amplitudes, our estimate of  $u_{\text{post}}(t)$  seems to describe some of the unmodelled annual and semi-annual oscillations (e.g. Figure 3).

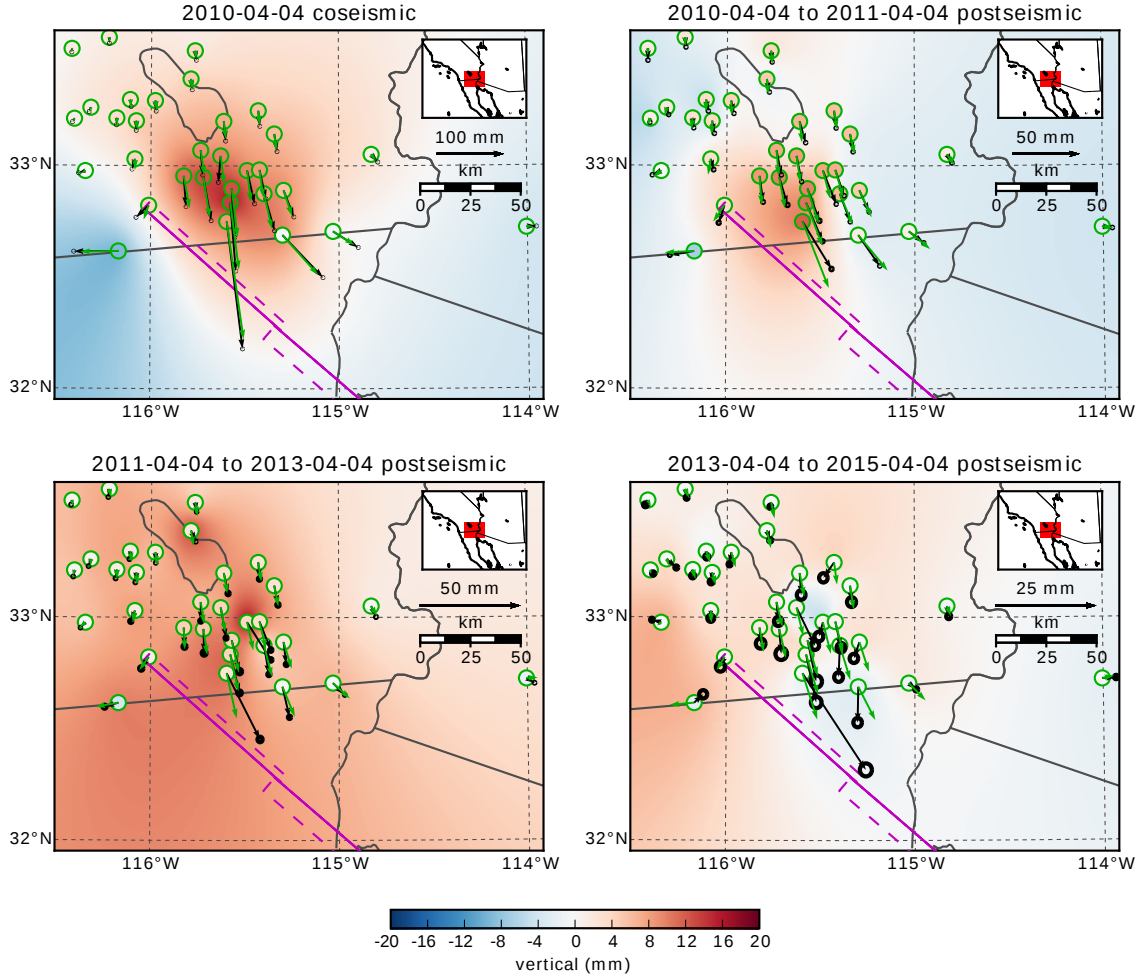
We show in Figures 4 and 5 the near and far-field postseismic displacements accumulated over the time intervals 0-1 years, 1-3 years, and 3-5 years, as well as the coseismic displacements. Stations at epicentral distances ranging from  $\sim 200$  km to as far as  $\sim 400$  km have an elevated rate of deformation for the first 3 years following the earthquake. This far-field deformation has a southward trend along the direction of the El Mayor-Cucapah P axis and a similar eastward trend can be seen in the few far-field stations in Arizona, located along the T axis. After 3 years, the trend in far-field postseismic deformation is barely perceptible. The vertical deformation in the far-field is difficult to attribute to postseismic processes. Most far-field stations display an initial subsidence for the first year after the El Mayor-Cucapah earthquake followed by continued uplift. This trend in vertical deformation can be observed in all



153 **Figure 2.** Left panels show GPS time series from UNAVCO (black) and the predicted displacement (blue)  
 154 from eq. (2) for a near-field station. Red lines indicate the times of the El Mayor-Cucapah and Ocotillo earth-  
 155 quakes. The right panels show estimated coseismic and postseismic displacements,  $u_{\text{post}}$ , which are extracted  
 156 from the predicted displacements. The 68% confidence interval is shown in light blue.



157 **Figure 3.** same as Figure 2 but for a far-field station.



183 **Figure 4.** Near-field coseismic and cumulative postseismic displacements over the indicated time periods  
 184 (black) as well as predicted displacements for our preferred model from Section 3.3 (green). Observed verti-  
 185 cal deformation is shown as an interpolated field and predicted vertical displacements are shown within the  
 186 circles at the base of each vector. Note that the interpolant is not well constrained in Mexico where there is no  
 187 data available.

178 three of the quadrants where postseismic data is available, which means that the vertical de-  
 179 formation does not exhibit an anti-symmetric quadrant pattern, as would be expected for post-  
 180 seismic processes. Although we use vertical deformation in our analysis in Section 3, we do  
 181 not put an emphasis on trying to describe the vertical deformation as it likely does not have  
 182 postseismic origins.

189 The near-field postseismic deformation is notably sustained when compared to the far-  
 190 field deformation. Namely, the station in this study which is closest to the El Mayor-Cucapah  
 191 epicentre, P496, has been moving at a steady rate of  $\sim 1.5$  cm/yr to the south since  $\sim 1$  year  
 192 after the El Mayor-Cucapah earthquake. Vertical postseismic deformation in the near-field does  
 193 display a quadrant pattern which is consistent with the coseismic vertical deformation, sug-  
 194 gesting that it is resulting from tectonic processes. However, the vertical postseismic signal  
 195 is only apparent for the first year after the earthquake (Figure 4). As with the far-field defor-  
 196 mation, there is a general trend of uplift in the near-field after  $\sim 1$  year, which we do not con-  
 197 sider to be related to postseismic processes.

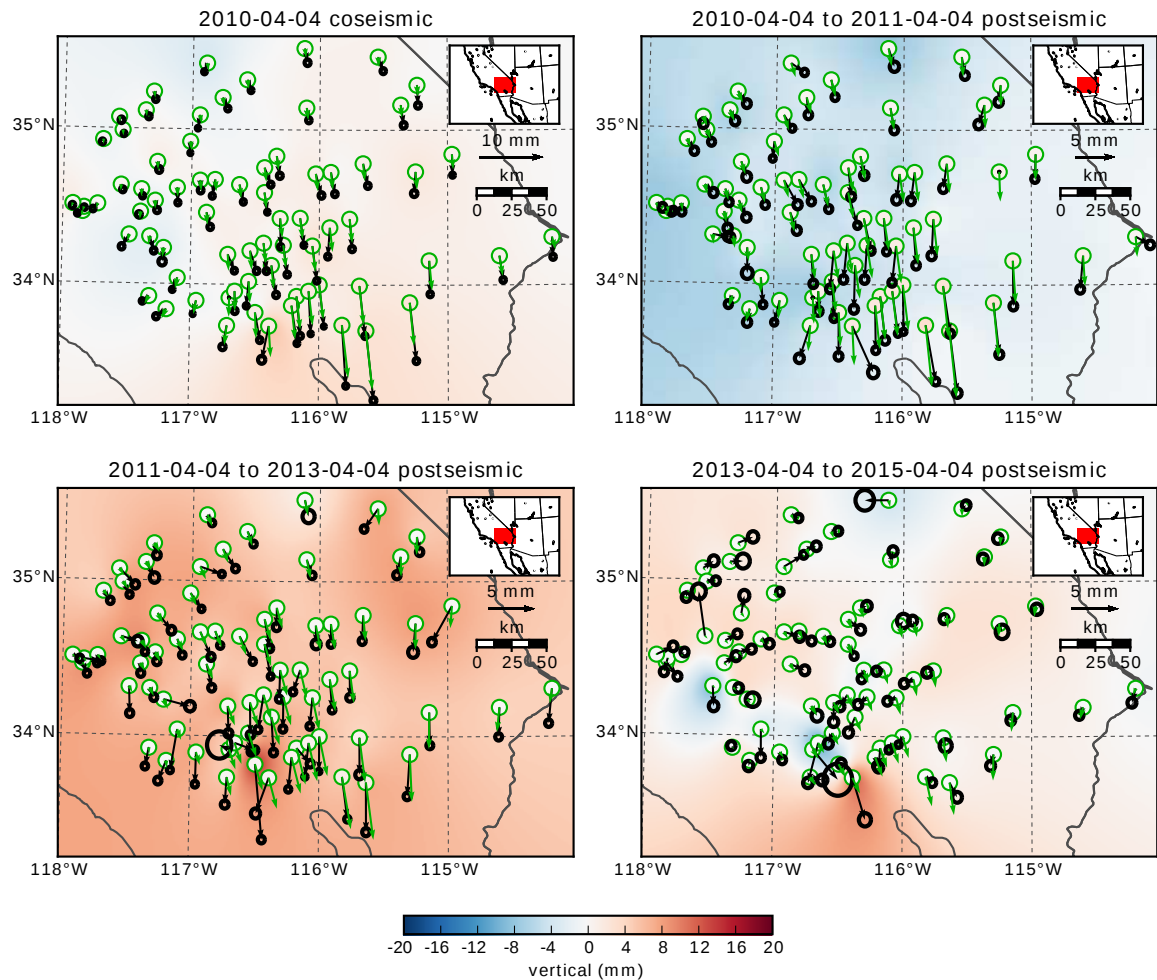


**Figure 5.** Same as Figure 4 but for far-field stations.

depth (km)	$\lambda$ (GPa)	$\mu$ (GPa)	$\eta_{\text{eff}}$ ( $10^{18}$ Pa s)	$\mu_k/\mu$
0-5	24.0	24.0	-	-
5-15	35.0	35.0	-	-
15-30	42.0	42.0	44.3	0.0
30-60	61.0	61.0	5.91	0.375
60-90	61.0	61.0	1.99	0.375
90-120	61.0	61.0	1.31	0.375
120-150	61.0	61.0	1.10	0.375
150- $\infty$	61.0	61.0	1.07	0.375

**Table 1.** Assumed and estimated material properties.  $\lambda$  and  $\mu$  are assumed known *a priori* and are based on the values used for the coseismic model by *Wei et al.* [2011b]. The values for  $\eta_{\text{eff}}$  are estimated in Section 3.2 and  $\frac{\mu_k}{\mu}$  are the optimal shear moduli ratios found in Section 3.3 for a Zener rheology upper mantle.

### 3 Postseismic Modeling

In this paper, we seek to find the mechanisms driving 5 years of postseismic deformation following the El Mayor-Cucapah earthquake. We consider afterslip and viscoelastic relaxation in the lithosphere and asthenosphere as candidate mechanisms. Poroelastic rebound has also been used to model postseismic deformation [e.g. Jónsson *et al.*, 2003]; however, *Gonzalez-Ortega et al.* [2014] found that poroelastic rebound is unlikely to be a significant contributor to postseismic deformation following the El Mayor-Cucapah earthquake. Furthermore, we consider stations which are sufficiently far away from the main rupture that poroelastic rebound should be insignificant.

We estimate coseismic and time-dependent postseismic fault slip, both of which are assumed to occur on a fault geometry modified from *Wei et al.* [2011b]. Field studies [*Fletcher et al.*, 2014] and LIDAR observations [*Oskin et al.*, 2012] have revealed a significantly more complicated fault geometry than what was inferred by *Wei et al.* [2011b], especially within the Sierra Cucapah. However, we find that a relatively simple coseismic fault geometry based on [*Wei et al.*, 2011b] is adequate because most of the stations used in this study are sufficiently far from the El Mayor-Cucapah rupture zone that they are insensitive to the details in the fault geometry found by *Fletcher et al.* [2014] and *Oskin et al.* [2012]. The fault geometry used in this study (Figure 1) consists of the two main fault segments inferred by *Wei et al.* [2011b], where the northern segment runs through the Sierra Cucapah up to the US-Mexico border and the southern segment is the Indiviso fault which extends down to the Gulf of California. Both segments extend from the surface to 15 km depth. We extend the northern segment by 40 km to the north-west, motivated by the clustering of aftershocks on the northern tip of the coseismic rupture zone [*Hauksson et al.*, 2011; *Kroll et al.*, 2013]. This extended fault segment was also found to be necessary by *Rollins et al.* [2015] and *Pollitz et al.* [2012] in order to describe the postseismic deformation.

#### 3.1 elastic inversion

We consider a variety of rheologic models for the lower crust and upper mantle. The simplest rheologic model is to consider them to be effectively elastic and isotropic. In such case, the rheologic parameters consist of the Lamé parameters,  $\lambda$  and  $\mu$ , which are reasonably well known and we use the same values used by *Wei et al.* [2011b], which are listed in Table 3, throughout this paper. The only unknown is the distribution of fault slip, which can be easily estimated from postseismic deformation through linear least squares. Using a subset of the GPS stations considered in this study, *Rollins et al.* [2015] found that 3 years of postseismic deformation following the El Mayor-Cucapah earthquake can be explained with afterslip on the coseismic fault plane without requiring any viscoelastic relaxation. We also perform

an elastic slip inversion, but we use GPS stations within a larger radius about the El Mayor-Cucapah epicentre (400 km instead of  $\sim 200$  km). Our forward problem describing predicted postseismic deformation,  $u_{\text{pred}}$ , in terms of time dependent fault slip,  $s$ , is

$$u_{\text{pred}}(x, t) = \int_F s(\xi, t)g(x, \xi)d\xi \quad (9)$$

where  $g(x, \xi)$  is elastic Green's function describing displacement at surface position  $x$  resulting from a unit of slip at  $\xi$  on the fault, which is denoted by  $F$ . We estimate coseismic slip and the rate of afterslip at the discrete time intervals, 0.0-0.125, 0.125-0.25, 0.5-1.0, 1.0-2.0, 2.0-3.0, 3.0-4.0, and 4.0-5.0 years after the earthquake. Each fault segment is discretized into roughly 4 km by 4 km patches and we estimate a strike-slip and thrust component of slip for each patch. We impose that the direction of slip and slip rate are within  $45^\circ$  of right-lateral. We also add zeroth order Tikhonov regularization so that our solution for  $s$  satisfies

$$\min_s \left( \left\| \frac{u_{\text{pred}}(s) - u_{\text{post}}}{\sigma_{\text{obs}}} \right\|_2^2 + \lambda_s \|s\|_2^2 \right). \quad (10)$$

The penalty parameters,  $\lambda_s$ , is chosen with a trade-off curve. We use Pylith [Aagaard *et al.*, 2009] to compute the Green's functions for this inversion, as well as for the remaining inversions in this paper.

Our coseismic slip and afterslip solutions are shown in Figure 6. As with Rollins *et al.* [2015], we find that a large amount of afterslip on the southern fault segment is required to explain the observations. The potency of our inferred coseismic slip is  $3.2 \times 10^9 \text{ m}^3$ , equivalent to a Mw7.28 earthquake when assuming a shear modulus of 32 GPa. The potency of our inferred cumulative 5 years of afterslip is  $6.1 \times 10^9 \text{ m}^3$ , equivalent to a Mw7.46 earthquake, which is unrealistically large if we consider afterslip to be driven by coseismically induced stresses. Our elastic slip model accurately describes near-field postseismic deformation, while it systematically underestimates postseismic deformation for stations further than  $\sim 150$  km from the El Mayor-Cucapah epicentre (Figure 7). When the fault segments used in the inversion are extended down to 30 km depth, rather than 15 km, the systematic far-field residuals are smaller but remain apparent. Because an elastic model for the lithosphere requires an unrealistic amount of afterslip and is unable to predict far-field deformation, we move on to consider viscoelastic models in the next section.

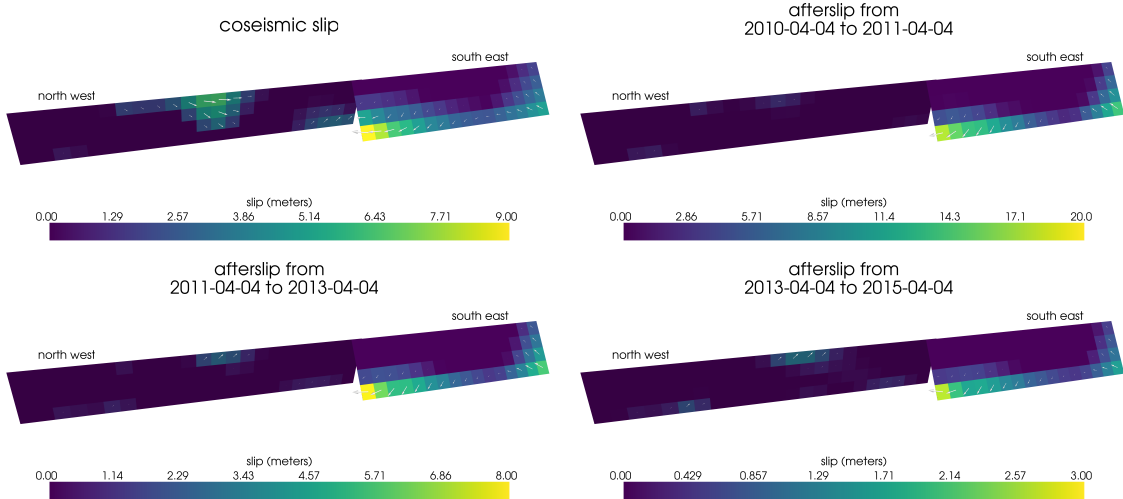
### 3.2 constraints on effective viscosity

For any linear viscoelastic rheology of the crust and mantle, postseismic displacements resulting from time dependent fault slip can be described as

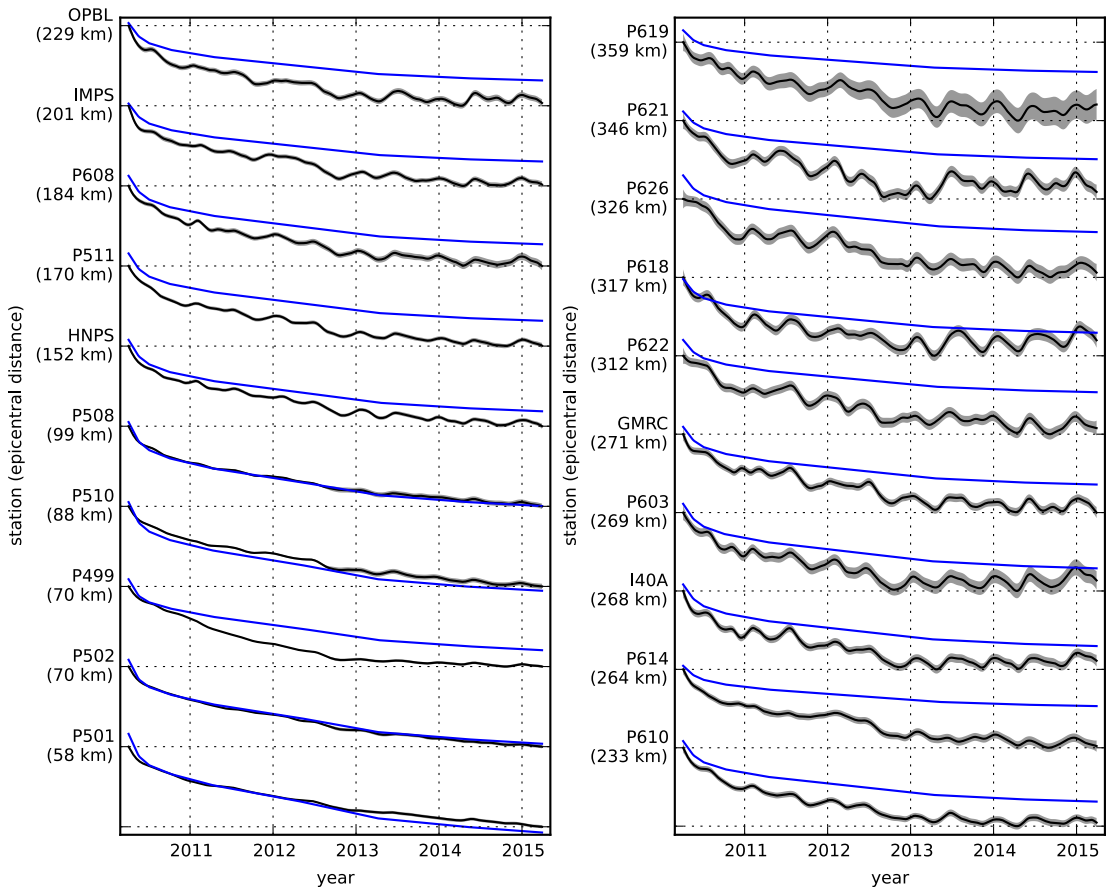
$$u_{\text{pred}}(x, t) = \int_F s(\xi, t)g(x, \xi)d\xi + \int_0^t \int_F s(\xi, \tau)f(t - \tau, x, \xi)d\xi d\tau \quad (11)$$

where  $f(t, x, \xi)$  describes the time-dependent velocity at  $x$  resulting from viscoelastic relaxation of stresses induced by slip at  $\xi$ .  $f$  is a function of  $\lambda$ ,  $\mu$ , and any additional rheologic parameters controlling the viscoelastic response, which are generally not well known. Schematic representations of the viscoelastic rheologic models considered in this study are shown in Figure 8. We consider Maxwell viscoelasticity, where the steady-state viscosity,  $\eta_M$ , is unknown, Zener viscoelasticity, where the transient viscosity,  $\eta_K$ , and transient shear modulus,  $\mu_K$ , are unknown, and Burgers viscoelasticity, where  $\eta_M$ ,  $\eta_K$ , and  $\mu_K$ , are all unknown. We further discuss these rheologic models and their use in geophysical studies in Section 4.

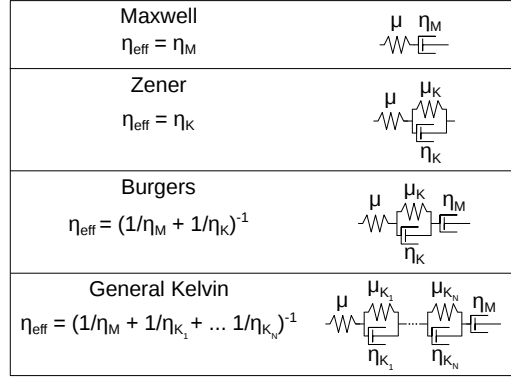
In order to greatly simplify the inverse problem, we use the method described in Hines and Hetland [2016] to constrain an initial effective lithospheric viscosity structure from the early postseismic deformation. The method relies upon the fact that immediately after an earthquake, stresses throughout the crust and mantle are only controlled by the relatively well known instantaneous elastic properties and each parcel will have a strain rate,  $\dot{\epsilon}$ , that is proportional



243 **Figure 6.** Coseismic slip and cumulative afterslip over the indicated intervals for the elastic model from  
244 Section 3.1. Color indicates the magnitude of slip while arrows indicate the motion of the hanging wall.



245 **Figure 7.** Scaled record section for the radial component of observed postseismic displacements,  $u_{\text{obs}}$   
246 (black) and displacements predicted by an elastic model,  $u_{\text{pred}}$  (blue). Downward motion indicates that the  
247 station is moving toward the El Mayor-Cucapah epicentre. Displacement time series are scaled so that the  
248 minimum and maximum observed values lie on the grid lines. The standard deviation of observed displace-  
249 ments are shown in gray.



259 **Figure 8.** Schematic illustration of rheologic models considered in this paper as well as their initial effec-  
 260 tion viscosities,  $\eta_{\text{eff}} = \frac{\sigma}{\dot{\epsilon}}|_{t=0}$ .

to stress,  $\sigma$ , and inversely proportional to the parcel's effective viscosity,  $\eta_{\text{eff}} = \frac{\sigma}{\dot{\epsilon}}|_{t=0}$ . Through linear superposition, we can deduce that the initial rate of surface deformation resulting from viscoelastic relaxation is a summation of the surface deformation resulting from each parcel, scaled by the reciprocal of the parcel's effective viscosity. That is to say

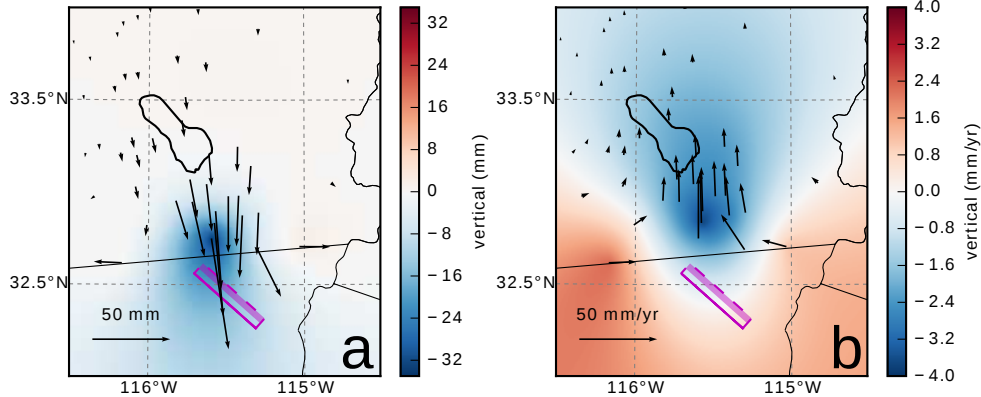
$$f(0, x, \xi) = \int_L \frac{h(x, \xi, \zeta)}{\eta_{\text{eff}}(\zeta)} d\zeta, \quad (12)$$

where  $h(x, \xi, \zeta)$  describes the initial rate of deformation resulting from viscoelastic relaxation at  $\zeta$  induced by slip at  $\xi$  and  $L$  denotes the crust and mantle. We can combine eq. (12) with eq. (11) to get a first order approximation for early postseismic deformation,

$$u_{\text{pred}}(x, t) \approx \int_F s(\xi, t) g(x, \xi) d\xi + \int_0^t \int_F \int_L \frac{s(\tau, \xi)}{\eta_{\text{eff}}(\zeta)} h(x, \xi, \zeta) d\zeta d\xi d\tau, \quad (13)$$

261 which is valid for as long as the rate of deformation resulting from viscoelastic relaxation is  
 262 approximately constant. Although eq. (13) may only be valid for a short portion of the post-  
 263 seismic period, its utility becomes apparent when noting that  $g$  and  $h$  are only functions of  
 264 the fault geometry and instantaneous elastic properties,  $\lambda$  and  $\mu$ , and so  $g$  and  $h$  can be com-  
 265 puted numerically as a preprocessing step and the forward problem in eq. (13) can be rapidly  
 266 evaluated for any realization of  $s$  and  $\eta_{\text{eff}}$ . This is in contrast to evaluating the full forward  
 267 problem, eq. (11), numerically for each realization of  $s$  and unknown rheologic properties. Fig-  
 268 ure 8 shows how estimates of  $\eta_{\text{eff}}$  can then be used as a constraint on the unknown param-  
 269 eters for various linear viscoelastic rheologies.

270 We perform an initial inversion of postseismic displacements using the approximation  
 271 in eq. (13). We estimate coseismic slip and afterslip with the same spatial and temporal dis-  
 272 cretization as in Section 3.1. Simultaneously, we estimate  $\eta_{\text{eff}}$  within six vertically stratified  
 273 layers which have depths ranging from 15-30 km, 30-60 km, 60-90 km, 90-120 km, 120-150  
 274 km, as well as from 150 km to the bottom of our numerical model domain at 800 km. We again  
 275 restrict fault slip to occur between 0 and 15 km depth and we made this choice to help elim-  
 276 inate inevitable non uniqueness. It has long been recognized that fault slip at sufficiently great  
 277 depths can produce surface deformation that is indistinguishable from viscoelastic relaxation,  
 278 at least in two-dimensional earthquake models [Savage, 1990]. Since we are trying to sim-  
 279 ultaneously model these two processes, it is necessary to put sensible constraints on the depth  
 280 of fault slip. Additionally, we note that when simultaneously estimating afterslip in the lower  
 281 crust and a lower crustal viscosity, the inverse problem becomes particularly ill-posed. This  
 282 ill-posedness is illustrated in Figure (9), which shows the displacements resulting from a me-  
 283 ter of slip on a fault extending from 15 to 30 km depth and the initial velocity resulting from



294 **Figure 9.** Displacements resulting from fault slip at lower crustal depths (left), and initial velocity resulting  
 295 in subsequent relaxation of a viscoelastic lower crust (right). The fault segment dips  $75^\circ$  to the north  
 296 east and its surface projection is outlined in green. The highlighted area on the fault extends from 15 to 30  
 297 km depth and indicates where 1 meter of right-lateral slip was imposed. The elastic properties of the crust  
 298 and mantle are the same as in Table 3 and  $\eta_{\text{eff}} = 10^{18}$  Pa s in the lower crust. Vertical displacements are  
 299 interpolated between station locations.

284 viscoelastic relaxation in the lower crust, which is given a viscosity of  $10^{18}$  Pa s. The hori-  
 285 zontal displacements from fault slip are in the opposite direction as the displacements result-  
 286 ing from subsequent viscoelastic relaxation. This means that surface displacements resulting  
 287 from afterslip at lower crustal depths can be cancelled out, at least partially, by a low visco-  
 288 elastic viscosity lower crust. We eliminate this null space by allowing only one mechanism in the lower crust,  
 289 which we choose to be viscoelastic relaxation. This is not to say that we do not believe deep  
 290 afterslip to be a possibility, rather we restrict slip to seismogenic depths as a modelling ne-  
 291 cessity. Although, it has been noted that the pattern of vertical postseismic deformation fol-  
 292 lowing the El Mayor-Cucapah earthquake indicates that a significant amount of afterslip must  
 293 be shallow [Rollins et al., 2015].

300 Further details on how  $s$  and  $\eta_{\text{eff}}$  are estimated from postseismic deformation can be found  
 301 in Hines and Hetland [2016]. A non-linear Kalman filter based inverse method can also be used  
 302 to estimate  $s$  and  $\eta_{\text{eff}}$  in a manner akin to Segall and Mathews [1997] or McGuire and Segall  
 303 [2003], in which we would not have to explicitly impose a time dependent parametrization of  
 304  $s$ . We have thoroughly explored Kalman filter based approaches, but we ultimately prefer the  
 305 method described in Hines and Hetland [2016] because of its relative simplicity. Moreover,  
 306 we believe the piecewise continuous representation of slip with respect to time to be sufficiently  
 307 general for the resolving power of these GPS data.

308 The first step in our inverse method is to determine at which point the early postseis-  
 309 mic approximation breaks down, which we will denote as  $t_{\text{bd}}$ . As noted, it is valid for approx-  
 310 imately as long as the rate of deformation resulting from viscoelastic relaxation is approxi-  
 311 mately constant. We can almost certainly assume that deformation at the most far-field sta-  
 312 tions, which are  $\sim 400$  km away from the El Mayor-Cucapah epicentre, is the result of vis-  
 313 coelastic relaxation. The approximation should then be valid for as long as a linear trend ad-  
 314 equately approximates the far-field deformation. Using this logic, it would appear that  $t_{\text{bd}} \approx$   
 315 1 year after the El Mayor-Cucapah earthquake. Another way to determine  $t_{\text{bd}}$  is to find the  
 316 best fitting prediction of eq. (13) to observed deformation using increasing durations of the  
 317 postseismic time series.  $t_{\text{bd}}$  should be the point when eq. (13) is no longer capable of describ-  
 318 ing the observed deformation without incurring systematic misfits. This is illustrated in Fig-  
 319 ure 10, which show the scaled radial components of displacement for stations along the El Mayor-  
 320 Cucapah P axis. When using eq. (13) to fit the entire 5 years of postseismic displacement we

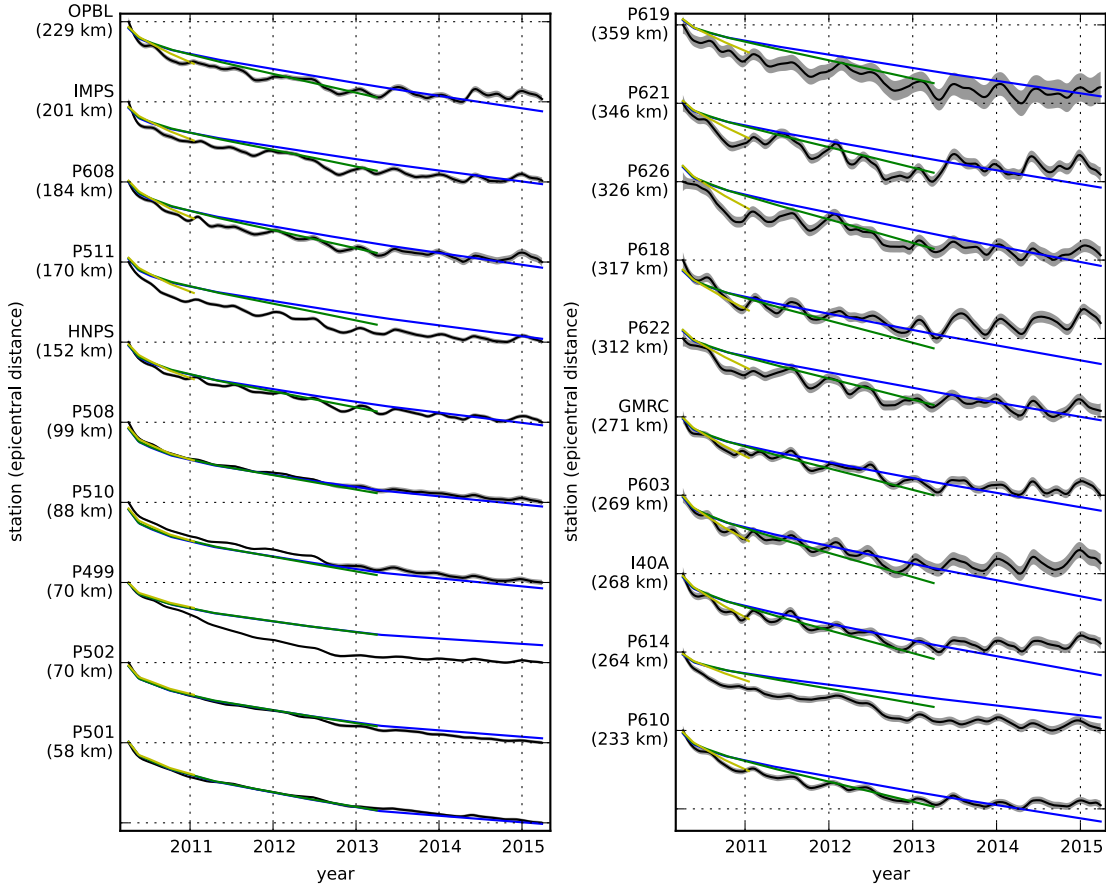


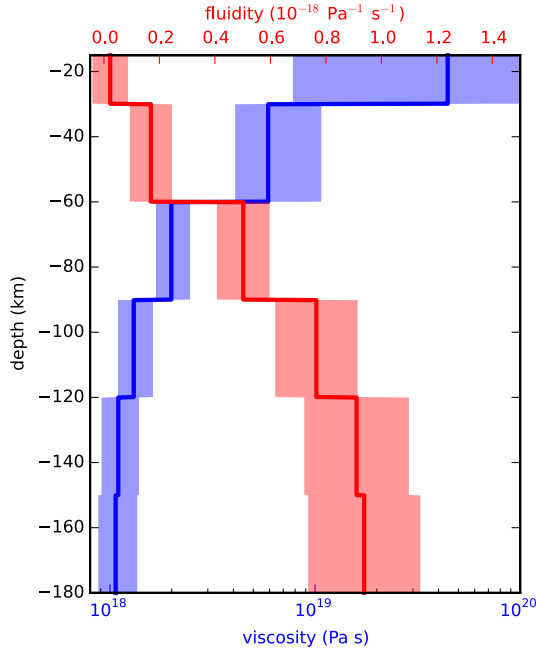
**Figure 10.** Illustration of how  $t_{bd}$  is chosen. Observed postseismic displacements are shown in black. Blue, green and yellow lines are the best fitting predictions to 5.0, 3.0, and 0.8 years of the postseismic data, respectively, from eq. 13.

see that the near-field displacements, e.g. station P501, are accurately predicted but when looking at displacement in the far-field, e.g. station P621, we see that eq. (13) overestimates the rate of deformation in the later postseismic period and underestimates the rate of deformation in the early period. Due to the low signal-to-noise ratios for far-field stations, it is difficult to determine at what point eq. (13) is no longer able to predict the observed displacements without incurring any significant systematic misfit; however, we settle on  $t_{bd} = 0.8$  years after the earthquake, while acknowledging that the choice is subjective. As noted in *Hines and Helland* [2016], overestimating  $t_{bd}$  will result in a bias towards overestimating  $\eta_{eff}$ , while picking a  $t_{bd}$  which is too low will not necessarily result in a biased estimate of  $\eta_{eff}$ , although the uncertainties would be larger. We can then consider inferences of  $\eta_{eff}$  to be an upper bound on the viscosity needed to describe the far-field rate of deformation during the first 0.8 years of postseismic deformation.

We estimate coseismic slip, afterslip, and effective viscosity by solving

$$\min_{s, \eta_{eff}} \left( \left\| \frac{u_{pred}(s, \eta_{eff}) - u_{obs}}{\sigma_{obs}} \right\|_2^2 + \lambda_s \|s\|_2^2 + \lambda_\eta \|\nabla \eta_{eff}^{-1}\|_2^2 \right) \quad (14)$$

where  $u_{obs}$  consists of the first 0.8 years of postseismic deformation and  $u_{pred}$  are the predicted displacements from eq. (13). Due to inherent non uniqueness, we have added zeroth order Tikhonov regularization to estimates of  $s$ , and second order Tikhonov regularization to

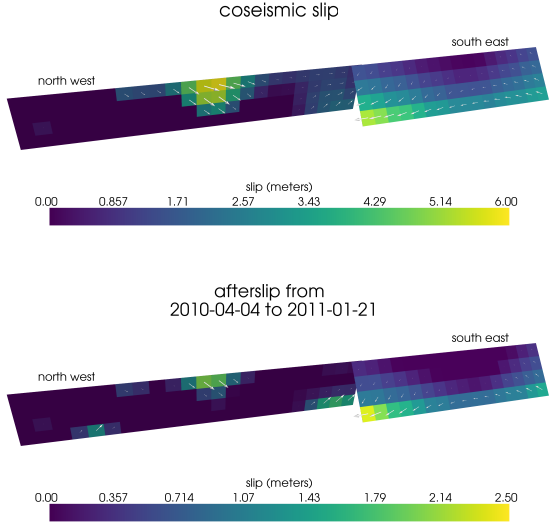


365 **Figure 11.** Effective viscosity and associated fluidities inferred by fitting eq. (13) to the first 0.8 years of  
366 postseismic displacements. 95% confidence intervals, estimated from bootstrapping, are also shown.

339 estimates of effective fluidity,  $\eta_{\text{eff}}^{-1}$ . The degree to which we impose the regularization on slip  
340 and fluidity is controlled by the penalty parameters  $\lambda_s$  and  $\lambda_\eta$ . The penalty parameters are cho-  
341 sen with two trade-off curves. We first choose  $\lambda_s$  while fixing  $\lambda_\eta$  at 0 and then we determine  
342  $\lambda_\eta$  with  $\lambda_s$  fixed at its chosen value. Our goal here is to get a prior constraint on  $\eta_{\text{eff}}$  to min-  
343 imize the amount of searching we have to do when describing the postseismic deformation over  
344 the full 5 years, which we do in Section 3.3. Estimates of  $s$  made here will not be used in Sec-  
345 tion 3.3, and so the motivation behind even adding regularization to  $s$  is to ensure that the slip  
346 driving viscoelastic relaxation in eq. (13) is sensible.

347 Our inferred estimates of effective viscosities, and corresponding fluidities, are shown  
348 in Figure 11 with their 95% confidence intervals indicated, which were estimated through boot-  
349 strapping. Although fluidity is rarely used in geophysical literature, eq. (12) is linear with re-  
350 spect to fluidity and so the fluidity indicates the amplitude of the viscoelastic signal coming  
351 from each layer. We note that the magnitude of the uncertainties on viscosity tend to decrease  
352 as we increase  $\lambda_\eta$ . Our choice of  $\lambda_\eta$  was based on a standard technique used in geophysical  
353 inverse problems which has no statistical backing. It is therefore difficult to interpret the mag-  
354 nitude of uncertainties on viscosities shown in Figure 11; although, we do believe that the rel-  
355 ative uncertainty between layers is accurately depicted. A robust feature that we see is that  
356 the largest jump in fluidity is at 60 km depth, which is consistent with the range of lithosphere-  
357 asthenosphere boundary depths inferred by Lekic *et al.* [2011]. This transitional depth is also  
358 consistent with the the viscosity structure required to explain far field postseismic deforma-  
359 tion following the Hector Mine earthquake [Freed *et al.*, 2007]. We find that the viscosity be-  
360 low 60 km depth needs to be  $\sim 1 \times 10^{18}$  Pa s to describe the early rate of postseismic defor-  
361 mation at far-field stations while the lower crust and uppermost mantle need to be relatively  
362 stronger. The viscosity of the lower crust is the least well constrained as there is no evidence  
363 of relaxation in that layer, meaning that it is effectively elastic over the first 0.8 years after the  
364 earthquake.

367 Our initial estimate for coseismic slip and cumulative afterslip over the first 0.8 years  
368 after the El Mayor-Cucapah earthquake are shown in Figure 12. Similar to our elastic slip model



384 **Figure 12.** Coseismic slip and afterslip inferred by fitting eq. (13) to the first 0.8 years of postseismic  
385 displacements.

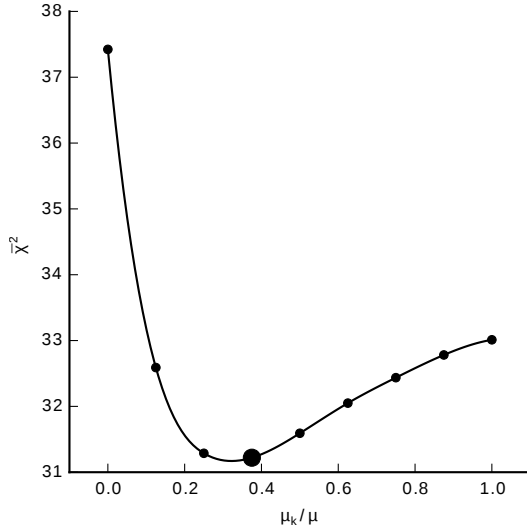
369 from Section 3.1, coseismic slip is inferred to be in the Sierra Cucapah and it is right lateral  
370 with a significant normal component. This is consistent with field studies [Fletcher *et al.*, 2014],  
371 as well as the coseismic slip from Wei *et al.* [2011b]. The potency of inferred coseismic slip  
372 is  $3.3 \times 10^9 \text{ m}^3$ , which is also about the same as that inferred from Section 3.1. The present  
373 inference of afterslip on the Indiviso fault is significantly less than what was found in the Sec-  
374 tion 3.1 where we did not account for viscoelasticity. When fault slip is simultaneously es-  
375 timated with a lithospheric and asthenospheric viscosity, the potency of inferred afterslip over  
376 the first 0.8 years after the earthquake is  $0.85 \times 10^9 \text{ m}^3$ , compared to  $3.46 \times 10^9 \text{ m}^3$  when  
377 we assume the lithosphere and asthenosphere are elastic. The significant amount of afterslip  
378 inferred on the Indiviso fault seems to be compensating for unmodelled viscoelastic relaxation  
379 at depths greater than 60 km. The fact that there is still an appreciable amount of afterslip in-  
380 ferred on the Indiviso fault even when allowing for viscoelastic relaxation in the lower crust  
381 and upper mantle raises the question of whether it is compensating for viscoelastic relaxation  
382 that is more localized than what we allow for since we only estimate depth dependent vari-  
383 ations in viscosity.

### 386 3.3 Full Inversion

In the previous section, we used the inverse method from Hines and Hetland [2016] to constrain the effective viscosity structure required to explain the first 0.8 years of postseismic deformation. In this section, we use the effective viscosities inferred above as a prior constraint when searching for models which are capable of describing the available 5 years of postseismic data, where our forward problem is now eq. (11) rather than the approximation given by eq. (13). We perform a series of coseismic slip and afterslip inversion assuming a variety of rheologies for the lower crust and upper mantle which are consistent with our findings from Section 3.2. We appraise each model using the mean chi squared value,

$$\bar{\chi}^2 = \frac{1}{N} \left\| \frac{u_{\text{pred}} - u_{\text{obs}}}{\sigma_{\text{obs}}} \right\|_2^2, \quad (15)$$

387 where  $N$  is the number of observations.

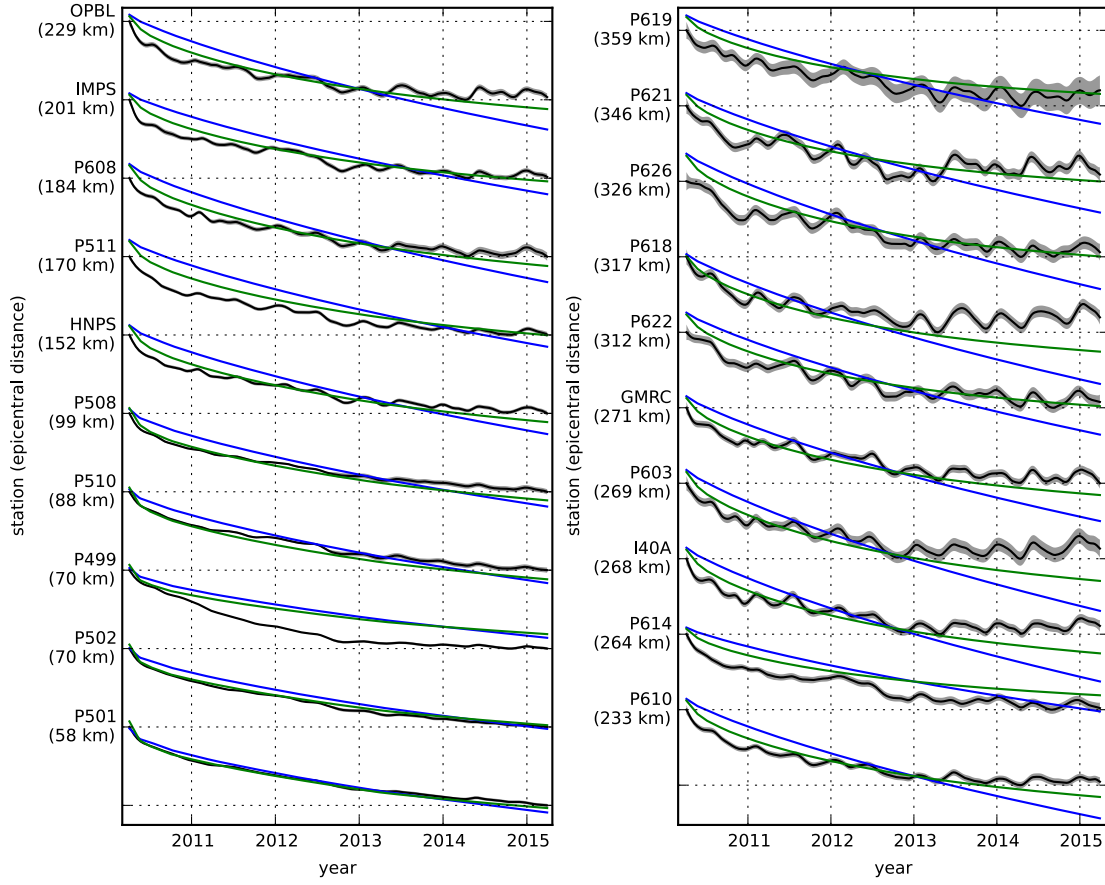


416 **Figure 13.** Misfit as a function of the transient shear modulus in a Zener rheology upper mantle.

388 We first assume that the crust and mantle can be described with a Maxwell rheology,  
 389 and we set  $\eta_M$  equal to our inference of  $\eta_{\text{eff}}$ . We compute  $f$  and  $g$  from eq. (11) using the  
 390 finite element software, Pylith [Aagaard *et al.*, 2009], and assume the same spatial and tem-  
 391 poral discretization of  $s$  as in Sections 3.1 and 3.2. We estimate  $s$  using linear least squares  
 392 and we find  $\bar{\chi}^2 = 37.4$ . For comparison,  $\bar{\chi}^2 = 35.3$  for the elastic model from Section 3.1.  
 393 The Maxwell viscoelastic model has a larger misfit because it tends to overestimate the rate  
 394 of deformation after about 3 years [14]. Since our initial estimates of  $\eta_{\text{eff}}$  may be biased towards  
 395 overestimating viscosities, we have also performed the slip inversion where we use uniformly  
 396 lower viscosities in the crust and mantle. However, decreasing the viscosity only increases the  
 397 misfit. Although, the viscosities used here are consistent with the successful Maxwell viscoelas-  
 398 tic models found by Rollins *et al.* [2015] and Spinler *et al.* [2015], which had mantle viscosi-  
 399 ties on the order of  $10^{18}$  Pa s, we find that such a model is incapable of describing the en-  
 400 tire postseismic time series. Pollitz *et al.* [2001] similarly recognized this deficiency in a Maxwell  
 401 rheology, which then motivated their exploration of a Burgers rheology upper mantle [Pollitz,  
 402 2003].

403 Rather than exploring a Burgers rheology mantle, which introduces two new parame-  
 404 ters that need to be estimated,  $\eta_K$  and  $\mu_K$ , we first consider a Zener rheology for the man-  
 405 tle, which only introduces the unknown parameter  $\mu_K$ . We assume that the lower crust still  
 406 has a Maxwell rheology. The steady-state viscosity,  $\eta_M$ , in the crust and the transient viscos-  
 407 ity,  $\eta_K$ , in the mantle are set equal to the inferred effective viscosities. We then estimate the  
 408 ratio of shear moduli,  $\frac{\mu_K}{\mu}$ . We compute nine different sets of Green's functions,  $f$  and  $g$ , us-  
 409 ing Pylith, where we assume values of  $\frac{\mu_K}{\mu}$  ranging from 0 to 1. The former being a degen-  
 410 erate case where the Zener model reduces to the above Maxwell model. We estimate coseis-  
 411 mic slip and afterslip for each realization of  $\frac{\mu_K}{\mu}$ . The shear moduli ratio that yields to best  
 412 prediction to the observed postseismic displacements is found to be 0.375 with a misfit of  $\bar{\chi}^2 =$   
 413 31.2 (Figure 13). The improvement in the Zener model over the Maxwell model can be clearly  
 414 seen in the fit to the far-field data (Figure 14). The Zener model does a significantly better job  
 415 at explaining the transient rate of far-field deformation throughout the 5 years.

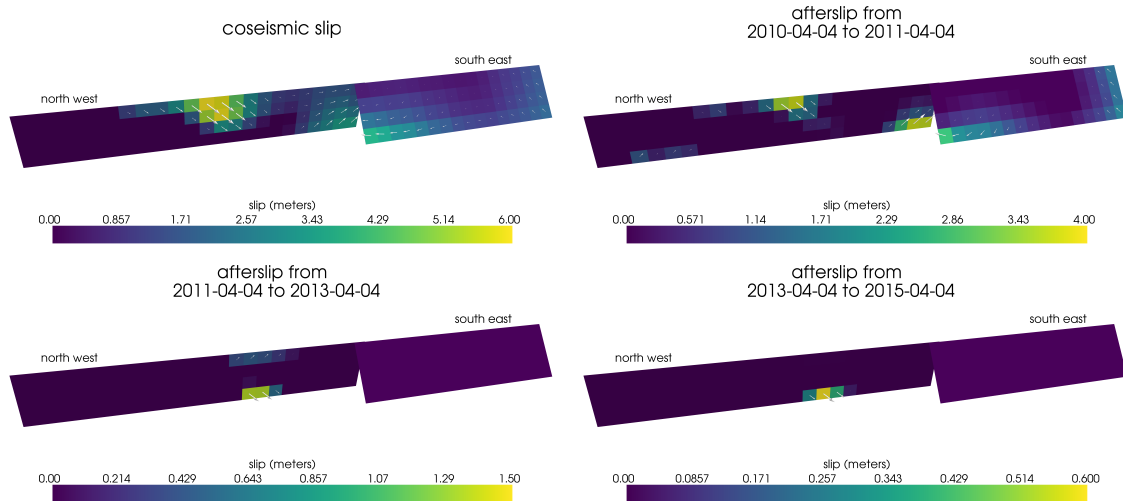
420 Because we are able to adequately describe the available 5 years of postseismic defor-  
 421 mation with a Zener model, we do not find it necessary to explore the parameter space for a  
 422 more complicated Burgers rheology. However, since the Zener model is a Burgers model with  
 423 an infinite steady-state viscosity, we can conclude that any Burgers rheology that has a tran-



417 **Figure 14.** Observed postseismic displacements (black) and predicted postseismic displacements for the  
 418 best fitting slip models when using a Maxwell (blue) and Zener (green) rheology in the upper mantle. The  
 419 effective viscosities are the same for both models and are shown in Figure 11.

424 transient viscosity consistent with that found in Section 3.2 and a steady-state viscosity of  $\gtrsim 10^{20}$   
 425 Pa s, which is effectively infinite on the time scale of 5 years, would also be able to satisfactorily describe the observable postseismic deformation.

427 The regularized inference of coseismic slip and afterslip for our preferred Zener model  
 428 is shown in Figure 15 and the predicted postseismic displacements are shown Figures 4, 5 and  
 429 14. Overall, the trends in the near-field and far-field transient deformation are accurately de-  
 430 scribed by our preferred model. In particular, the trends in far-field deformation are much bet-  
 431 ter described by our preferred Zener model than either an elastic model or a model with a Maxwell  
 432 viscoelastic mantle (Figure 14). There are a few areas where we have notable misfit. Most of  
 433 our misfit is for the near-field stations in the Imperial Valley, and we attribute this misfit to  
 434 our relatively simple fault geometry, which does not account for potential fault slip in the Im-  
 435 perial Valley triggered by the El Mayor-Cucapah earthquake [Wei *et al.*, 2011a, 2015]. In par-  
 436 ticular, we are unable to model the sustained rapid rate of deformation at station P496, which  
 437 suggests that this station could be influenced by a more localized deformation mechanism than  
 438 is considered in this study. Additionally, we see systematic misfit in the later postseismic pe-  
 439 riod west of the location of the Landers and Hector Mine earthquakes, which may be the re-  
 440 sult of unmodelled postseismic deformation resulting from those earthquakes. Lastly, there are  
 441 clear discrepancies between the observed and predicted vertical deformation following the first  
 442 year after the El Mayor Cucapah earthquake. We observe a broad uplift throughout Southern  
 443 California, which is inconsistent with any postseismic model.



444 **Figure 15.** Inferred coseismic slip and afterslip when assuming a Maxwell rheology in the lower crust  
 445 and a Zener rheology in the upper mantle.  $\eta_K$  in the mantle and  $\eta_M$  in the crust are set equal to the effective  
 446 viscosities from Figure 11. We use  $\frac{\mu_K}{\mu} = 0.375$  in the upper mantle.

447 The inferred coseismic potency is  $3.0 \times 10^9 \text{ m}^3$ , equivalent to a Mw7.26 earthquake,  
 448 and the potency of 5 years of afterslip is  $1.1 \times 10^9 \text{ m}^3$ . Most of the afterslip in our preferred  
 449 model occurs within the first year after the earthquake with a significant amount inferred to  
 450 be shallow and in the Sierra Cucapah. The afterslip within the first year is accounting for the  
 451 most rapid near-field transient deformation. After 1 year, afterslip is inferred to be deeper and  
 452 under the Sierra Cucapah, which is describing much of the sustained near-field postseismic  
 453 deformation. We emphasize, that the GPS station closest to our inferred afterslip, P496, is still  
 454 about 30 km away, which is too far away for us to conclusively argue for sustained brittle de-  
 455 formation rather shallow ductile deformation. The deep afterslip inferred after 1 year could  
 456 potentially be describing deformation resulting from lower crustal flow. To test this, we have

modified our preferred model by decreasing the lower crustal viscosity from  $5.91 \times 10^{19}$  Pa s to  $1 \times 10^{19}$  Pa s, which is still consistent with our viscosity inference from Section 3.2. After performing another slip inversion, we find that a model with a weaker lower crust adequately describes the postseismic displacements without any afterslip after 1 year, while still requiring about the same amount of afterslip over the first year. We do believe that the early shallow afterslip is a robust feature in our preferred model, while we are not confident in our inference of later deep afterslip.

## 4 Discussion

It has long been recognized that deep afterslip and viscoelastic relaxation following an upper crustal earthquake can result in similar horizontal ground deformation at the surface [e.g. Savage, 1990; Pollitz *et al.*, 2001; Hearn, 2003; Feigl and Thatcher, 2006]. The similarity of the horizontal postseismic deformation results in a non-uniqueness in inferences of afterslip or viscoelastic relaxation. In contrast, the spatial pattern of vertical postseismic deformation has been proposed to be a discriminant between deep afterslip and viscoelastic relaxation [e.g. Pollitz *et al.*, 2001; Hearn, 2003]. It is, however, important to note that patterns of vertical deformation are very sensitive to the depth-dependence of viscosity below the upper crust [?Hetland and Zhang, 2014]. The similarity between deformation resulting from deep afterslip and viscoelastic relaxation of coseismic stresses is different from the ill-posedness described in Section 3.2. In our method, any inferred afterslip will also mechanically drive additional viscoelastic relaxation. The horizontal deformation resulting from deep afterslip will generally be in the opposite direction as horizontal deformation resulting from viscoelastic relaxation of subsequent stresses in the lower crust (Figure 9). As a result, there is a trade-off between inferences of deep afterslip and lower crustal viscosity. In our synthetic tests in ?, we have found that inverting surface deformation for afterslip and viscosity within the same depth interval tends to result in overestimated afterslip and an underestimated viscosity at that depth.

Most postseismic studies assume Maxwell viscoelasticity in the lower crust and upper mantle [e.g. Nur and Mavko, 1974; Pollitz *et al.*, 2000; Hetland, 2003; Freed *et al.*, 2006; Johnson *et al.*, 2009; Hearn *et al.*, 2009], which is the simplest viscoelastic rheologic model. In Southern California, postseismic studies following the Landers [Pollitz *et al.*, 2000], Hector Mine [Pollitz *et al.*, 2001], and El Mayor-Cucapah earthquake [Spinler *et al.*, 2015; Rollins *et al.*, 2015], have assumed Maxwell viscoelasticity in the lithosphere and asthenosphere and have inferred upper mantle viscosities on the order of  $10^{17}$  to  $10^{18}$  Pa s and lower crust viscosities of  $\gtrsim 10^{19}$  Pa s. These postseismic studies are consistent with Kaufmann and Amelung [2000]; ? who found that an upper mantle viscosity of  $10^{18}$  Pa s and a crustal viscosity  $\gtrsim 10^{20}$  Pa s are necessary to describe subsidence resulting from Lake Mead, which is a process with similar spatial and temporal scales as postseismic deformation. While these studies found viscosities that are consistent with our effective viscosities from Section 3.2, they are inconsistent with viscosity estimates made from geophysical processes that occur over longer time scales. For example, Lundgren *et al.* [2009] found that lower crust and upper mantle viscosities on the order of  $10^{21}$  and  $10^{19}$  Pa s, respectively, are needed to describe interseismic deformation along the Southern San Andreas and San Jacinto fault. An even higher mantle viscosity on the order of  $10^{20}$  Pa s is required to describe deflection resulting from Lake Bonneville, which occurs on the time scales of  $10^4$  years [Crittenden, 1967; Bills and May, 1987].

An additional deficiency with the Maxwell rheology is that it predicts a steady decay over time in the rate of postseismic deformation, which fails to describe the commonly observed rapid early transience followed by a relatively steady rate of postseismic deformation. One could explain the early transient postseismic deformation with fault creep and the later phase with relaxation in a Maxwell viscoelastic lower crust and upper mantle [e.g Hearn *et al.*, 2009; Johnson *et al.*, 2009]. However, postseismic deformation at distances greater than  $\sim 200$  km from the El Mayor-Cucapah epicentre can only be attributed to viscoelastic relaxation [Freed *et al.*, 2007] and we have demonstrated that the far-field deformation cannot be explained with a Maxwell rheology (Figure 14).

We found that a Zener rheology in the upper mantle with a transient viscosity of  $\sim 10^{18}$  Pa s does a noticeably better job at predicting far-field postseismic deformation. A generalization of the Zener viscoelastic model, schematically represented as several Kelvin elements connected in series, is commonly used to describe seismic attenuation [Liu *et al.*, 1976]. The highest viscosity needed to describe seismic attenuation is on the order of  $10^{16}$  Pa s [Yuen and Peltier, 1982] which has a characteristic relaxation time on the order of days. Even though our inferred transient viscosity is orders of magnitude larger than that required for seismic attenuation models, the two models are not incompatible. Rather, the delayed elasticity in seismic attenuation models occurs on such short time scales that it can be considered part of the instantaneous elastic phase of deformation associated with the preferred Zener model in this study.

Of course, it has long been recognized that a Zener rheology provides an incomplete descriptions of the asthenosphere, as it does not have the fluid-like behaviour required to explain isostatic rebound or convection in the mantle [O'Connell, 1971]. Yuen and Peltier [1982] proposed a Burgers rheology with a low transient viscosity ( $\eta_K \approx 10^{16}$  Pa s) and high steady-state viscosity ( $\eta_M \approx 10^{21}$  Pa s) to describe both seismic attenuation and long term geologic processes. The justification of a Burger's rheology mantle is further supported by laboratory experiments on olivine [Chopra, 1997]. Pollitz [2003] sought to describe postseismic deformation following Hector Mine with a Burgers rheology mantle and they found a best fitting transient viscosity of  $1.6 \times 10^{17}$  Pa s and steady-state viscosity of  $4.6 \times 10^{18}$  Pa s. While the Burgers rheology was introduced as a means of bridging the gap between relaxation observed in long and short term geophysical processes, the inferred steady state viscosity from Pollitz [2003] is still inconsistent with the Maxwell viscosities inferred from earthquake cycle and lake loading studies. The transient viscosity inferred by Pollitz [2003] is constrained by the earliest phase of postseismic deformation following the Hector Mine earthquake. While Pollitz [2003] ruled out deep afterslip as an alternative mechanism based on inconsistent vertical deformation, it is still possible to successfully describe all components of early postseismic deformation following the Hector Mine earthquake with afterslip at seismogenic depths [Jacobs *et al.*, 2002]. It is then possible that the preferred rheologic model from Pollitz [2003] was biased towards inferring a particularly low transient viscosity by neglecting to account for afterslip. This is in contrast to the present study, where we have inferred a lithospheric viscosity structure simultaneously with afterslip. We also argue that a transient rheology is necessary to explain postseismic deformation; however, our preferred transient viscosity of  $\sim 10^{18}$  Pa s in the mantle is an order of magnitude larger than the transient viscosity found by Pollitz [2003]. Since a Zener model is able to describe the available postseismic deformation following the El Mayor-Cucapah earthquake, any Burgers rheology with a steady-state viscosity that is  $\gtrsim 10^{20}$  Pa s, effectively infinite over 5 years, would also be able to describe the postseismic deformation. Such a Burgers model might then be consistent with the steady state viscosities necessary for lake loading, interseismic deformation, and mantle dynamics.

## 5 Conclusion

We have extracted a filtered and smoothed estimate of postseismic deformation following the El Mayor-Cucapah earthquake from GPS displacements time series. We have treated postseismic deformation as a stochastic process where we did not presume any characteristic shape of the postseismic time series. We can observe transient postseismic deformation at distances of  $\sim 400$  km from the El Mayor-Cucapah epicenter which is largely undetectable after about 3 years. Near-field deformation exhibits transience that decays to a sustained, elevated rate after about 1 to 2 year. We found that the near-field transient deformation can be explained with shallow afterslip and the sustained rate of near field deformation can either be explained with continued afterslip or relaxation in a lower crustal with a viscosity of  $\sim 10^{19}$  Pa s. Far-field transient deformation can be more definitively ascribed to viscoelastic relaxation at depths greater than  $\sim 60$  km. Beneath that depth, a transient viscosity of  $\sim 10^{18}$  Pa s is required to describe the rate of far-field deformation throughout the 5 years considered in

561 this study. By describing the available postseismic deformation with a transient rheology in  
 562 the mantle, our preferred model does not conflict with the generally higher steady-state vis-  
 563 cosities inferred from geophysical processes occurring over longer time scales.

564 **Acknowledgements**

565 We are grateful to Andy Freed for an illuminating discussion on the material in this manuscript.

566 This material is based on EarthScope Plate Boundary Observatory data services provided  
 567 by UNAVCO through the GAGE Facility with support from the National Science Foundation  
 568 (NSF) and National Aeronautics and Space Administration (NASA) under NSF Cooperative  
 569 Agreement No. EAR-1261833.

570 This material is based upon work supported by the National Science Foundation under  
 571 Grant Numbers EAR 1045372 and EAR 1245263.

572 **Acknowledgments**

573 = enter acknowledgments here =

574 **References**

- 575 Aagaard, B., C. Williams, M. Knepley, S. Kientz, and L. Strand (2009), PyLith.  
 576 Argus, D. F., M. B. Heflin, G. Peltzer, F. Crampé, and F. H. Webb (2005), Interseismic  
 577 strain accumulation and anthropogenic motion in metropolitan Los Angeles, *Journal of*  
 578 *Geophysical Research B: Solid Earth*, 110(4), 1–26, doi:10.1029/2003JB002934.  
 579 Bawden, G. W., W. Thatcher, R. S. Stein, K. W. Hudnut, and G. Peltzer (2001), Tectonic  
 580 contraction across Los Angeles after removal of groundwater pumping effects., *Nature*,  
 581 412(August), 812–815, doi:10.1038/35090558.  
 582 Bills, B. G., and G. M. May (1987), Lake Bonneville: Constraints on Lithospheric Thick-  
 583 ness and Upper Mantle Viscosity From Isostatic Warping of Bonneville, Provo, and  
 584 Gilbert Stage Shorelines, *Journal of Geophysical Research-Solid Earth and Planets*,  
 585 92(B11), 11,493–11,508, doi:10.1029/JB092iB11p11493.  
 586 Çakir, Z., S. Ergintav, H. Özener, U. Dogan, A. M. Akoglu, M. Meghraoui, and  
 587 R. Reilinger (2012), Onset of aseismic creep on major strike-slip faults, *Geology*,  
 588 40(12), 1115–1118, doi:10.1130/G33522.1.  
 589 Cetin, E., Z. Çakir, M. Meghraoui, S. Ergintav, and A. M. Akoglu (2014), Extent and  
 590 distribution of aseismic slip on the İsmetpaşa segment of the North Anatolian Fault  
 591 (Turkey) from Persistent Scatterer InSAR, *Geochemistry, Geophysics, Geosystems*, 15,  
 592 doi:10.1002/2014GC005307.Received.  
 593 Chopra, P. N. (1997), High-temperature transient creep in olivine rocks, *Tectonophysics*,  
 594 279, 93–111, doi:10.1016/S0040-1951(97)00134-0.  
 595 Crittenden, M. (1967), Viscosity and Finite Strength of the Mantle as Determined from  
 596 Water and Ice Loads\*, *Geophysical Journal of the Royal Astronomical ...*, pp. 261–279,  
 597 doi:10.1111/j.1365-246X.1967.tb06243.x.  
 598 Davis, J. L., B. P. Wernicke, and M. E. Tamisiea (2012), On seasonal signals in geode-  
 599 tic time series, *Journal of Geophysical Research: Solid Earth*, 117(1), 1–10, doi:  
 600 10.1029/2011JB008690.  
 601 Feigl, K. L., and W. Thatcher (2006), Geodetic observations of post-seismic transients in  
 602 the context of the earthquake deformation cycle, *Comptes Rendus - Geoscience*, 338,  
 603 1012–1028, doi:10.1016/j.crte.2006.06.006.  
 604 Fletcher, J. M., O. J. Teran, T. K. Rockwell, M. E. Osokin, K. W. Hudnut, K. J. Mueller,  
 605 R. M. Spelz, S. O. Akciz, E. Masana, G. Faneros, E. J. Fielding, S. Leprince, A. E.  
 606 Morelan, J. Stock, D. K. Lynch, A. J. Elliott, P. Gold, J. Liu-Zeng, A. González-  
 607 Ortega, A. Hinojosa-Corona, and J. González-García (2014), Assembly of a large

- 608 earthquake from a complex fault system: Surface rupture kinematics of the 4 April  
 609 2010 El Mayor-Cucapah (Mexico) Mw 7.2 earthquake, *Geosphere*, 10(4), 797–827,  
 610 doi:10.1130/GES00933.1.
- 611 Freed, A. M., R. Bürgmann, E. Calais, J. Freymueller, and S. Hreinsdóttir (2006), Impli-  
 612 cations of deformation following the 2002 Denali, Alaska, earthquake for postseismic  
 613 relaxation processes and lithospheric rheology, *Journal of Geophysical Research: Solid*  
 614 *Earth*, 111, 1–23, doi:10.1029/2005JB003894.
- 615 Freed, A. M., R. Bürgmann, and T. Herring (2007), Far-reaching transient motions after  
 616 Mojave earthquakes require broad mantle flow beneath a strong crust, *Geophysical*  
 617 *Research Letters*, 34, 1–5, doi:10.1029/2007GL030959.
- 618 Gonzalez-Ortega, A., Y. Fialko, D. Sandwell, F. A. Nava-pichardo, J. Fletcher,  
 619 J. Gonzalez-garcia, B. Lipovsky, M. Floyd, and G. Funning (2014), El Mayor-  
 620 Cucapah (Mw7.2) earthquake: early near-field postseismic deformation from In-  
 621 Sar and GPS observations, *Journal of Geophysical Research*, 119, 1482–1497, doi:  
 622 10.1002/2013JB010193.Received.
- 623 Hauksson, E., J. Stock, K. Hutton, W. Yang, J. A. Vidal-Villegas, and H. Kanamori  
 624 (2011), The 2010 Mw 7.2 El mayor-cucapah earthquake sequence, Baja Califor-  
 625 nia, Mexico and Southernmost California, USA: Active seismotectonics along the  
 626 Mexican pacific margin, *Pure and Applied Geophysics*, 168(3918), 1255–1277, doi:  
 627 10.1007/s00024-010-0209-7.
- 628 Hearn, E. H. (2003), What can GPS data tell us about the dynamics of post-seismic defor-  
 629 mation ?, (2003), 753–777.
- 630 Hearn, E. H., S. McClusky, S. Ergintav, and R. E. Reilinger (2009), Izmit earthquake post-  
 631 seismic deformation and dynamics of the North Anatolian Fault Zone, *Journal of Geo-  
 632 physical Research: Solid Earth*, 114(August 2008), 1–21, doi:10.1029/2008JB006026.
- 633 Hetland, E. A. (2003), Postseismic relaxation across the Central Nevada Seismic Belt,  
 634 *Journal of Geophysical Research*, 108(Figure 2), 1–13, doi:10.1029/2002JB002257.
- 635 Hetland, E. A., and G. Zhang (2014), Effect of shear zones on post-seismic deformation  
 636 with application to the 1997 Mw 7.6 manyi earthquake, *Geophysical Journal Interna-  
 637 tional*, 198, 259–269, doi:10.1093/gji/ggu127.
- 638 Hines, T. T., and E. A. Hetland (2013), Bias in estimates of lithosphere viscosity from  
 639 interseismic deformation, *Geophysical Research Letters*, 40(16), 4260–4265, doi:  
 640 10.1002/grl.50839.
- 641 Hines, T. T., and E. A. Hetland (2016), Rapid and simultaneous estimation of fault slip  
 642 and heterogeneous lithospheric viscosity from post-seismic deformation, *Geophysical*  
 643 *Journal International*, 204(1), 569–582, doi:10.1093/gji/ggv477.
- 644 Jacobs, A., D. Sandwell, Y. Fialko, and L. Sichoix (2002), The 1999 (Mw7.1) Hector  
 645 Mine, California, Earthquake: Near-Field Postseismic Deformation from ERS Interfer-  
 646 ometry, *Bulletin of the Seismological Society of America*, 92(May), 1433–1442.
- 647 Johnson, K. M., and P. Segall (2004), Viscoelastic earthquake cycle models with deep  
 648 stress-driven creep along the San Andreas fault system, *Journal of Geophysical Research*  
 649 *B: Solid Earth*, 109, 1–19, doi:10.1029/2004JB003096.
- 650 Johnson, K. M., R. Bürgmann, and J. T. Freymueller (2009), Coupled afterslip and vis-  
 651 coelastic flow following the 2002 Denali Fault, Alaska earthquake, *Geophysical Journal*  
 652 *International*, 176(3), 670–682, doi:10.1111/j.1365-246X.2008.04029.x.
- 653 Jónsson, S., P. Segall, R. Pedersen, and G. Bjornsson (2003), Post-earthquake ground  
 654 movements correlated to pore-pressure transients, *Nature*, 424(July), 179–183, doi:  
 655 10.1038/nature01758.1.
- 656 Kaufmann, G., and F. Amelung (2000), Reservoir-induced deformation and continental  
 657 rheology in vicinity of Lake Mead, Nevada, *Journal of Geophysical Research*, 105(B7),  
 658 16,341, doi:10.1029/2000JB900079.
- 659 Kroll, K. A., E. S. Cochran, K. B. Richards-Dinger, and D. F. Sumy (2013), Aftershocks  
 660 of the 2010 Mw 7.2 El Mayor-Cucapah earthquake reveal complex faulting in the Yuha  
 661 Desert, California, *Journal of Geophysical Research: Solid Earth*, 118(October), 6146–

- 662 6164, doi:10.1002/2013JB010529.
- 663 Lekic, V., S. W. French, and K. M. Fischer (2011), Lithospheric Thinning Beneath Rifted  
664 Regions of Southern California, *Science*, 334(November), 783–787.
- 665 Liu, H.-P., D. L. Anderson, and H. Kanamori (1976), Velocity dispersion due to anelastic-  
666 ity; implications for seismology and mantle composition, *Geophysical Journal Interna-*  
667 *tional*, 47(1), 41–58, doi:10.1111/j.1365-246X.1976.tb01261.x.
- 668 Lundgren, P., E. A. Hetland, Z. Liu, and E. J. Fielding (2009), Southern San Andreas-San  
669 Jacinto fault system slip rates estimated from earthquake cycle models constrained by  
670 GPS and interferometric synthetic aperture radar observations, *Journal of Geophysical*  
671 *Research: Solid Earth*, 114(2), 1–18, doi:10.1029/2008JB005996.
- 672 McGuire, J. J., and P. Segall (2003), Imaging of aseismic fault slip transients recorded  
673 by dense geodetic networks, *Geophysical Journal International*, 155(3), 778–788, doi:  
674 10.1111/j.1365-246X.2003.02022.x.
- 675 Meade, B. J., and B. H. Hager (2005), Block models of crustal motion in southern Cal-  
676 ifornia constrained by GPS measurements, *Journal of Geophysical Research B: Solid*  
677 *Earth*, 110, 1–19, doi:10.1029/2004JB003209.
- 678 Murray, J. R., and P. Segall (2005), Spatiotemporal evolution of a transient slip event on  
679 the San Andreas fault near Parkfield, California, *Journal of Geophysical Research : Solid*  
680 *Earth*, 110(9), 1–12, doi:10.1029/2005JB003651.
- 681 Nur, A., and G. Mavko (1974), Postseismic viscoelastic rebound, *Science*, 183(4121),  
682 204–206, doi:10.1038/098448b0.
- 683 O'Connell, R. J. (1971), Rheology of the Mantle, *EOS, Transactions, American Geophysi-*  
684 *cal Union*, 52, 140–142.
- 685 Oskin, M. E., J. R. Arrowsmith, A. Hinojosa Corona, A. J. Elliott, J. M. Fletcher, E. J.  
686 Fielding, P. O. Gold, J. J. Gonzalez Garcia, K. W. Hudnut, J. Liu-Zeng, and O. J. Teran  
687 (2012), Near-field deformation from the El Mayor-Cucapah earthquake revealed by  
688 differential LIDAR, *Science*, 335(6069), 702–705, doi:10.1126/science.1213778.
- 689 Pollitz, F., C. Wicks, and W. Thatcher (2001), Mantle Flow Beneath a Continental Strike-  
690 Slip Fault : Postseismic Deformation After the 1999 Hector Mine Earthquake, *Science*,  
691 1814(2001), 1814–1818, doi:10.1126/science.1061361.
- 692 Pollitz, F. F. (2003), Transient rheology of the uppermost mantle beneath the Mo-  
693 jave Desert, California, *Earth and Planetary Science Letters*, 215, 89–104, doi:  
694 10.1016/S0012-821X(03)00432-1.
- 695 Pollitz, F. F., G. Peltzer, and R. Bürgmann (2000), Mobility of continental mantle: Evi-  
696 dence from postseismic geodetic observations following the 1992 Landers earthquake,  
697 *Journal of Geophysical Research*, 105(1999), 8035, doi:10.1029/1999JB900380.
- 698 Pollitz, F. F., R. Bürgmann, and W. Thatcher (2012), Illumination of rheological mantle  
699 heterogeneity by the M7.2 2010 El Mayor-Cucapah earthquake, *Geochemistry, Geo-*  
700 *physics, Geosystems*, 13(6), 1–17, doi:10.1029/2012GC004139.
- 701 Rauch, H. E., F. Tung, and C. T. Striebel (1965), Maximum likelihood estimates of linear  
702 dynamic systems, *AIAA Journal*, 3(8), 1445–1450.
- 703 Riva, R. E. M., and R. Govers (2009), Relating viscosities from postseismic relaxation to  
704 a realistic viscosity structure for the lithosphere, *Geophysical Journal International*, 176,  
705 614–624, doi:10.1111/j.1365-246X.2008.04004.x.
- 706 Rollins, C., S. Barbot, and J.-P. Avouac (2015), Postseismic Deformation Following the  
707 2010 M7.2 El Mayor-Cucapah Earthquake : Observations , Kinematic Inversions , and  
708 Dynamic Models, *Pure and Applied Geophysics*, doi:10.1007/s00024-014-1005-6.
- 709 Savage, J. C. (1990), Equivalent strike-slip earthquake cycles in half-space and  
710 lithosphere-asthenosphere earth models, *Journal of Geophysical Research*, 95, 4873,  
711 doi:10.1029/JB095iB04p04873.
- 712 Savage, J. C., and J. L. Svart (2009), Postseismic relaxation following the 1992 M 7.3  
713 Landers and 1999 M 7.1 Hector Mine earthquakes , southern California, *Journal of*  
714 *Geophysical Research*, 114(B01401), doi:10.1029/2008JB005938.

- 715 Savage, J. C., J. L. Svarc, and S. B. Yu (2005), Postseismic relaxation and transient creep,  
716 *Journal of Geophysical Research: Solid Earth*, 110, 1–14, doi:10.1029/2005JB003687.
- 717 Segall, P., and M. Mathews (1997), Time dependent inversion of geodetic data, *Journal of*  
718 *Geophysical Research*, 102.
- 719 Spinler, J. C., R. A. Bennett, C. Walls, L. Shawn, and J. J. G. Garcia (2015), Assess-  
720 ing long-term postseismic deformation following the M7.2 4 April 2010, El  
721 Mayor-Cucapah earthquake with implications for lithospheric rheology in the  
722 Salton Trough, *Journal of Geophysical Research: Solid Earth*, 120, 3664–3679, doi:  
723 10.1002/2014JB011613.Received.
- 724 Wei, M., D. Sandwell, Y. Fialko, and R. Bilham (2011a), Slip on faults in the Imperial  
725 Valley triggered by the 4 April 2010 Mw 7.2 El Mayor-Cucapah earthquake revealed by  
726 InSAR, *Geophysical Research Letters*, 38(January), 1–6, doi:10.1029/2010GL045235.
- 727 Wei, M., Y. Liu, Y. Kaneko, J. J. McGuire, and R. Bilham (2015), Dynamic triggering of  
728 creep events in the Salton Trough, Southern California by regional M5.4 earthquakes  
729 constrained by geodetic observations and numerical simulations, *Earth and Planetary  
730 Science Letters*, 427, 1–10, doi:10.1016/j.epsl.2015.06.044.
- 731 Wei, S., E. Fielding, S. Leprince, A. Sladen, J.-P. Avouac, D. Helmberger, E. Hauksson,  
732 R. Chu, M. Simons, K. Hudnut, T. Herring, and R. Briggs (2011b), Superficial sim-  
733 plicity of the 2010 El MayorCucapah earthquake of Baja California in Mexico, *Nature  
734 Geoscience*, 4(9), 615–618, doi:10.1038/ngeo1213.
- 735 Yuen, D. A., and W. R. Peltier (1982), Normal modes of the viscoelastic earth, *Geo-  
736 physical Journal of the Royal Astronomical Society*, 69, 495–526, doi:10.1111/j.1365-  
737 246X.1982.tb04962.x.